Pump-probe cavity optomechanics with a rotating atomic superfluid in a ring

Sampreet Kalita,[1] Pardeep Kumar,[2,*] Rina Kanamoto,[3] M. Bhattacharya,[4] and Amarendra K. Sarma[1]
[1]*Department of Physics, Indian Institute of Technology Guwahati, Guwahati, Assam 781039, India*
[2]*Max Planck Institute for the Science of Light, Staudtstraße 2, 91058 Erlangen, Germany*
[3]*Department of Physics, Meiji University, Kawasaki, Kanagawa 214-8571, Japan*
[4]*School of Physics and Astronomy, Rochester Institute of Technology, 84 Lomb Memorial Drive, Rochester, New York 14623, USA*

(Received 30 July 2022; revised 29 December 2022; accepted 11 January 2023; published 26 January 2023)

Atomic superfluids confined in a ring provide a remarkable paradigm for quantized circulation. Very recently, a technique based on cavity optomechanics has been proposed [Kumar *et al.*, Phys. Rev. Lett. **127**, 113601 (2021)] for sensing and manipulating the rotation of a bosonic ring condensate with minimal destruction, *in situ* and in real time. Here, we theoretically investigate other coherent interference effects that can be supported by the proposed configuration. Specifically, in the presence of a strong control beam, we analyze the influence of atomic rotation on the transmission spectrum of a weak probe laser through a cavity containing a ring condensate. We present a detailed study of the resulting narrow probe transmission profiles and group delay and show that they can be tuned by means of persistent currents. Our results explore a facet of rotating matter waves and are relevant to applications such as atomtronics, sensing, and information processing.

DOI: 10.1103/PhysRevA.107.013525

I. INTRODUCTION

In recent years, annularly trapped [1] Bose-Einstein condensates (BECs) have emerged as a remarkable system for studying a plethora of phenomena [2–7] associated with quantized circulation [8]. Such systems support quantized vortices for macroscopically long times [9–11] and topologically stabilized states of higher circulation [12] thus providing a versatile platform for investigations of superfluid hydrodynamics [13,14], matter-wave interferometry [15], atomtronic circuits [16,17], and fermionic superfluidity [18–20].

For the studies mentioned above, it is very important to characterize the circulation of the ring condensate. The determination of the rotation of an atomic superfluid typically requires the measurement of the phase (winding number) of a rotational state. The existing techniques for detecting the winding number involve atomic absorption of the photons used for imaging, and are thus fully destructive, thus precluding real-time observation and placing requirements on the replication of initial conditions [2]. Also the radius of the vortex (i.e., ring trap) is typically smaller than the optical wavelength, thereby making it difficult to perform *in situ* detection of vortices in the trapped dilute gases, and requiring time-of-flight expansion techniques [4].

To circumvent the above issues, very recently, a versatile system [21] was proposed to sense and manipulate the rotation of an annular BEC with minimal destruction, *in situ* and in real time. This method utilizes the technique of cavity optomechanics, a unique platform for exploring the interaction of mechanical systems with light fields confined inside an optical resonator [22]. Interestingly, the method improves the rotation sensitivity of ring BECs by three orders of magnitude compared with demonstrated methods and also provides a way to manipulate atomic currents by generating optomechanical entanglement between atomic matter waves.

In this paper, we investigate a different way to manipulate the interaction of optical beams carrying orbital angular momentum (OAM) with an annular BEC confined inside a cavity to realize coherent effects. Specifically, within the paradigm of rotational optomechanics [23], we examine the modification, by a rotating atomic superfluid, of the destructive interference between a strong pump field and a weak probe field driving the cavity containing the superfluid.

The three main findings of our work are as follows: (i) Working under resonant conditions, destructive interference results in the emergence of symmetric narrow transmission windows in the probe spectrum. For instance, in the absence of quantized circulation, the system exhibits optomechanically induced transparency (OMIT) [24–29], an effect analogous to electromagnetically induced transparency [30–33]. However, in the presence of atomic superflow the probe transmission spectrum is modified, and a double-OMIT structure appears with an absorption window at the resonance. Moreover, the characteristic features of the output probe spectrum can be manipulated by tuning the quantized circulation. For instance, we find that the location difference of the absorption dips in the probe transmission profile

*pardeep.kumar@mpl.mpg.de

becomes sensitive to the magnitude of the winding number. The separation between such dips thus provides a useful tool for establishing the magnitude of the quantized circulation. (ii) However, under nonresonant conditions the probe output spectrum exhibits asymmetric transmission profiles known as Fano resonances [34,35]. The asymmetry in the probe transmission spectrum depends on the winding number of the ring BEC. (iii) In addition to modifying the transmission, the destructive interference also affects the dispersion. Specifically, the transmission window is accompanied by a positive group delay (slow light) while the absorption window accompanies a negative group delay (fast light). In our system the transmission window turns into absorption in the presence of atomic rotation. Consequently, we find that switching from slow to fast light can be accomplished by introducing ring BEC rotation. Considering these observations, our system could find potential applications in various sectors such as quantum state transfer protocols [36,37], measurement of OAM of light [38], optical switching [39,40], and wavelength conversion [41].

The paper is organized as follows: In Sec. II, we discuss the formalism of the system from an optomechanical perspective and derive a general expression for the transmission amplitudes of the optical field in phase and out of phase with the probe frequency. In Sec. III, we then study the probe transmission and group delay. Finally, we conclude by discussing its applications and future directions in Sec. IV.

II. MODEL

We consider an atomic BEC [sodium (Na)] of N atoms confined in a ring trap of radius R placed inside an optical cavity as shown in Fig. 1, and rotating with a winding number L_p. For such a configuration, the potential experienced by each atom in the condensate is such that the motion decouples along radial (ρ), axial (z), and azimuthal (ϕ) directions. We employ a one-dimensional description of the problem, i.e., we consider the dynamics only along the azimuthal direction by assuming that the quantum state along radial and axial directions remains unchanged throughout the dynamic evolution of the system. Such a one-dimensional description can be applied [42] if $N < \frac{4\sqrt{\pi}R}{3a_{\rm Na}}(\frac{\omega_\rho}{\omega_z})^{1/2}$. Here, $a_{\rm Na}$ and ω_ρ (ω_z) are the ground-state scattering length of the Na atoms and the radial (axial) harmonic trapping frequency, respectively.

A superposition of two control lasers of frequency ω_{lc} and power P_{lc} carrying OAM $\pm l\hbar$ interacts with the condensate. The generation of such a coaxial OAM superposition has already been achieved experimentally [43–45]. The corresponding optical beams generate an angular lattice inside the cavity and cause Bragg scattering of some atoms in the condensate. For a weak dipole potential [21], only the first-order diffraction needs to be considered [see bottom panel of Fig. 1(a)], namely, scattering from the rotational state with winding number L_p to states with winding number $L_p \pm 2l$. We now introduce a weak laser drive of frequency ω_{lp} and power P_{lp} to probe the ring-BEC–cavity system.

Using the above arguments and the fact that the dynamics of the macroscopically occupied state with winding number

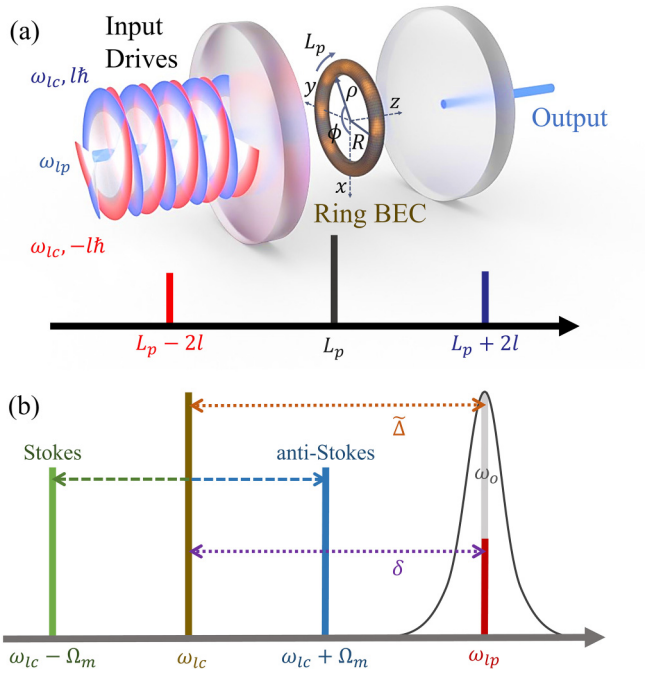

FIG. 1. (a) Top: A Fabry-Pérot cavity with partially reflecting mirrors is driven by coherent control beams (red and blue helices on the left) carrying OAM, which interact with a toroidally trapped BEC. A second weak laser (light blue beams) probes the cavity, and the transmission spectrum at the probe frequency is measured at the output. Bottom: Position of the Bragg-scattered side modes on either side of the initial BEC winding number. (b) Illustration of the laser frequencies and the first mechanical sidebands of the control laser.

L_p is essentially classical, we write the following simplified form of the many-body Hamiltonian in the rotating frame of the control laser [21]:

$$\frac{H}{\hbar} = -\tilde{\Delta}a^\dagger a + \sum_{j=c,d}\frac{\omega_j}{2}\left(X_j^2 + Y_j^2\right) + G(X_c + X_d)a^\dagger a + \sum_{j=c,d} 2\tilde{g}N\left(X_j^2 + Y_j^2\right) + 2\tilde{g}N(X_cX_d - Y_cY_d) + i\eta_{lc}(a^\dagger - a) + i\eta_{lp}(a^\dagger e^{-i\delta t} - ae^{i\delta t}). \quad (1)$$

Here, the first term denotes the energy of the optical mode with $\tilde{\Delta} = \omega_{lc} - \omega_o - g_a^2N/(2\Delta_a)$, where ω_o, g_a, and Δ_a are the cavity frequency, the single atom-photon interaction strength, and the detuning of the laser frequency from the atomic transition, respectively; also, a and $a^\dagger$ are the annihilation and creation operators of the cavity field such that $[a, a^\dagger] = 1$. The second term denotes the energies of the side modes in terms of their dimensionless position and momentum operators given by $X_j = (j^\dagger + j)/\sqrt{2}$ and $Y_j = i(j^\dagger - j)/\sqrt{2}$, respectively. Here, $j = c, d$ (unless specified otherwise) are the bosonic atomic operators obeying $[j, j'^\dagger] = \delta_{jj'}$. Also, the side-mode frequencies [21] which are quadratic in angular momenta can be expressed as $\omega_c = \hbar(L_p + 2l)^2/(2I)$ and $\omega_d = \hbar(L_p - 2l)^2/(2I)$, where $I = mR^2$ is the atomic moment of inertia about the center of the ring trap. Here, m is the mass of each sodium atom. Note that the actual side-mode frequencies, from the Bogoliubov analysis, are given by

$\omega'_{c,d} = \sqrt{\omega^2_{c,d} + 4\omega_{c,d}\tilde{g}N}$. However, here we use $\omega'_{c,d} \sim \omega_{c,d}$ by imposing $\omega_{c,d} \gg 4\tilde{g}N$, where $\tilde{g} = g/4\pi\hbar$ corresponds to the scaled two-body atomic interactions, with $g = (2\hbar\omega_\rho a_{Na})/R$ [21]. Furthermore, the third term on the right-hand side of Eq. (1) denotes the optomechanical coupling between the side modes and the optical field where the effective side-mode coupling strength is given by $G = g_a^2\sqrt{N}/(2\sqrt{2}\Delta_a)$. The next two terms describe the intermode coupling owing to atom-atom interactions of strength $\tilde{g}$. The final two terms are the control laser field and the probe laser field entering the cavity, respectively, having amplitudes $\eta_{lk} = \sqrt{\mu\gamma_o P_{lk}/\hbar\omega_{lk}}$ with $k = c$ (p) for the control (probe) laser, the laser-cavity coupling parameter given by μ, and γ_o being the cavity linewidth. The detuning of the probe laser from the control laser is $\delta = \omega_{lp} - \omega_{lc}$.

In the presence of the probe field, the corresponding quantum Langevin equations (QLEs) for the system become

$$\dot{a} = -\left[\frac{\gamma_o}{2} - i\{\tilde{\Delta} - G(X_c + X_d)\}\right]a + \eta_{lc} + \eta_{lp}e^{-i\delta t} + \sqrt{\mu\gamma_o}a^{(in)}, \tag{2a}$$

$$\ddot{X}_c = -\gamma_m\dot{X}_c - \Omega_c^2 X_c - G\tilde{\omega}_c a^\dagger a - \mathcal{A}X_d + \omega_c\epsilon_c, \tag{2b}$$

$$\ddot{X}_d = -\gamma_m\dot{X}_d - \Omega_d^2 X_d - G\tilde{\omega}_d a^\dagger a + \mathcal{A}X_c + \omega_d\epsilon_d. \tag{2c}$$

Here, γ_m is the decay rate of the two side modes corresponding to the decay of supercurrents [46], $a^{(in)}$ is the zero-mean delta-correlated optical fluctuations entering the cavity [47], and ϵ_j represents the Brownian noise in the mechanical sidemodes [22]. Also, for the sake of simplicity, we have introduced the quantities $\Omega_j^2 = (\omega_j + 4\tilde{g}N)^2 - 4\tilde{g}^2N^2$ and $\tilde{\omega}_j = \omega_j + 2\tilde{g}N$, $\mathcal{A} = 2\tilde{g}N(\omega_c - \omega_d)$.

Below, we study the output spectra of the Stokes field, which is *in phase* with the probe frequency to determine its transparency and amplification windows. We begin by assuming that the probe field is *sufficiently weak* in comparison to the control field ($\eta_{lc} \gg \eta_{lp}$) so that its effect can be treated as a perturbation to the otherwise classical steady state. This, together with a sufficiently strong control field, allows us to present a linearized description of the system [47,48]. The primary motivation behind this linearization is to obtain a unique solution for the amplitudes of the time-varying optical field.

Considering that the main contributions in the transmission are from the first-order side modes of the probe field, the classical expectation values can be approximated as $\alpha = \langle a\rangle = \alpha_s + A_-e^{-i\delta t} + A_+e^{i\delta t}$, $q_c = \langle X_c\rangle = q_{cs} + C_-e^{-i\delta t} + C_+e^{i\delta t}$, and $q_d = \langle X_d\rangle = q_{ds} + D_-e^{-i\delta t} + D_+e^{i\delta t}$, where α_s, q_{cs}, and q_{ds} are the steady-state mode amplitudes in the *adiabatic limit* ($\gamma_o \gg \gamma_m, g_a^2/\Delta_a$) and are given by

$$\alpha_s = \eta_{lc}/(\gamma_o/2 - i\Delta), \tag{3a}$$

$$q_{cs} = -G\tilde{\omega}_d|\alpha_s|^2/\sqrt{\mathcal{A}^2 + \Omega_c^2\Omega_d^2}, \tag{3b}$$

$$q_{ds} = -G\tilde{\omega}_c|\alpha_s|^2/\sqrt{\mathcal{A}^2 + \Omega_c^2\Omega_d^2}, \tag{3c}$$

with effective detuning $\Delta = \tilde{\Delta} - G(q_{cs} + q_{ds})$. We thereby obtain the sideband amplitudes of the optical mode as

$$A_- = \frac{\eta_{lp}(\Gamma_+ + iG^2\Lambda|\alpha_s|^2)}{\Gamma_+\Gamma_- + 2\Delta G^2\Lambda|\alpha_s|^2}, \tag{4a}$$

$$A_+^* = \frac{-iG^2\eta_{lp}\Lambda(\alpha_s)^2}{\Gamma_+\Gamma_- + 2\Delta G^2\Lambda|\alpha_s|^2}, \tag{4b}$$

where $\Gamma_\pm = (\gamma_o/2 \pm i\Delta - i\delta)$, $\chi_j = 1/(\Omega_j^2 - i\delta\gamma_m - \delta^2)$, and $\Lambda = \{\mathcal{A}\chi_c\chi_d(\tilde{\omega}_c - \tilde{\omega}_d) + \chi_c\tilde{\omega}_c + \chi_d\tilde{\omega}_d\}/(\mathcal{A}^2\chi_c\chi_d + 1)$. Now, using the input-output formalism, $a_{\rm out} = -a_{\rm in} + \sqrt{\mu\gamma_o}a$, the expectation value of the cavity output field can be expressed as

$$\langle a_{\rm out}\rangle = s_{lc}e^{-i\omega_{lc}t} + s_S e^{-i(\delta+\omega_{lc})t} + s_{aS}e^{-i(\delta-\omega_{lc})t}. \tag{5}$$

In Eq. (5), $s_{lc} = \sqrt{\mu\gamma_o}\alpha_s - \frac{\eta_{lc}}{\sqrt{\mu\gamma_o}}$ is the signal at the control laser frequency ω_{lc}, and $s_S = \sqrt{\mu\gamma_o}A_- - \eta_{lp}/\sqrt{\mu\gamma_o}$ is the Stokes sideband signal oscillating at the frequency of the probe field $\delta + \omega_{lc} = \omega_{lp}$. In contrast, the anti-Stokes signal $s_{aS} = \sqrt{\mu\gamma_o}A_+$, which oscillates at $\omega_{lc} - \delta = 2\omega_{lc} - \omega_{lp}$, results in the four-wave mixing effect, due to the interaction of the upconverted control field and the reflected probe field. The above Stokes and anti-Stokes sidebands can also be visualized as the mechanical sidebands which arise due to the scattering of the strong control field. This can be seen in Fig. 1(b), when resonance condition $\delta = \Omega_m$ is achieved. Then the amplitude of the probe transmission is given by

$$t_S = \frac{s_S}{\eta_{lp}/\sqrt{\mu\gamma_o}}. \tag{6}$$

Here, the real and imaginary parts of the amplitude t_S reflect the absorption and dispersion properties of the optomechanical system in response to the probe field. Finally, using Eq. (6), the transmission at the probe frequency [24,25] is obtained as

$$T = |t_S|^2 = \left|1 - \frac{\mu\gamma_o A_-}{\eta_{lp}}\right|^2. \tag{7}$$

III. RESULTS

To investigate the effect of control-field-mediated interference on the output probe field, we choose experimentally feasible parameters [2,21,42,43,49–51]: $m = 23$ amu, $R = 10$ μm, $N = 10^4$, $\lambda_l = 589$ nm, $L_p = 1$ (unless stated otherwise), $l = 20$ (unless indicated otherwise), $g_a/2\pi = 0.36$ MHz, $\Delta_a/2\pi = 4.7$ GHz, depth of the optical potential $U_0/2\pi = 28.3$ Hz, $G/2\pi = 1$ kHz, $\gamma_m/2\pi = 0.8$ Hz, $\gamma_o/2\pi = 1$ kHz, $\mu = 0.5$, $a_{\rm Na} = 0.1$ nm, the atomic interaction in the mean-field regime ($\tilde{g}_m = \frac{\hbar}{4lN}$) $\tilde{g}_m/2\pi \sim 0.11$ mHz, $\tilde{g} \sim 12\tilde{g}_m$, and $\omega_z/2\pi = \omega_\rho/2\pi = 840$ Hz. Note that for the above parameters, our system is minimally destructive, namely, very few atoms get diffracted from the ring trap to first-order Bragg-diffraction side modes. Also, as stated in Sec. II, we have verified that this set of parameters satisfies (i) a one-dimensional description of our model, (ii) $\omega_{c,d} \gg 4\tilde{g}N$, and (iii) the inequality required for weak potential [21].

A. Stability analysis

To proceed further, we first choose the parameters for which the system remains monostable [21] and also satisfies

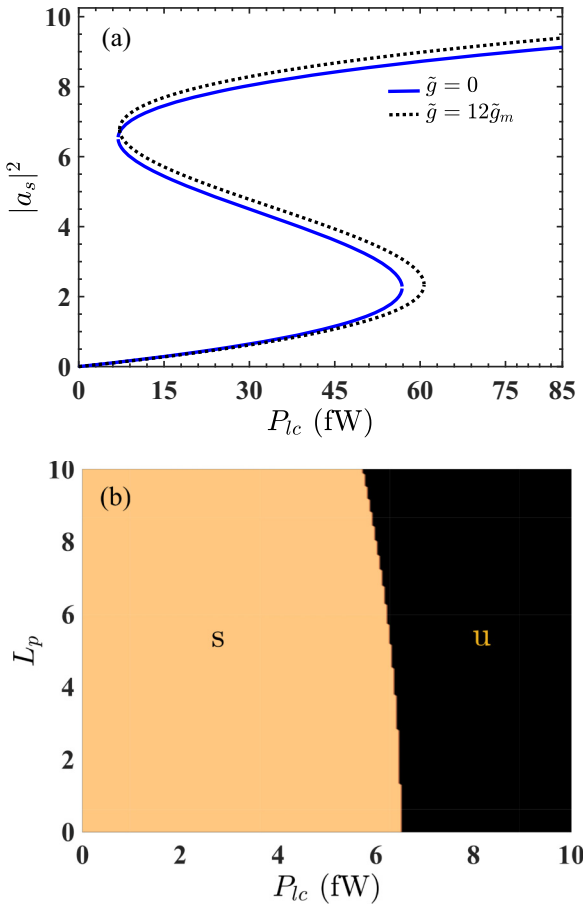

FIG. 2. (a) Bistability plot for $\tilde{g} = 0$ (solid blue curve) and $\tilde{g} = 12\tilde{g}_m$ (dotted black curve). (b) Stable (s) and unstable (u) regions of the system, according to the Routh-Hurwitz criterion mentioned in the text. All plots are obtained at $\tilde{\Delta} = -\Omega_m$.

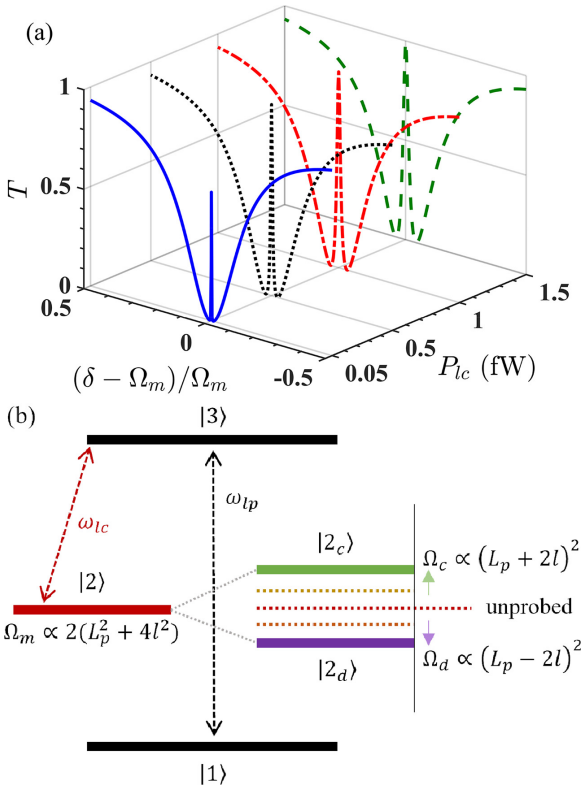

FIG. 3. (a) Transmission of the probe field for $L_p = 0$ obtained at $\tilde{\Delta} = -\Omega_m$. For this case the critical power is $\tilde{P}_{lc_{cr}} = 28$ fW. (b) Energy levels and transition pathways for the system at $\tilde{\Delta} = -\Omega_m$.

the Routh-Hurwitz criterion [52]. Also, we set the control field detuning equal to the mean of the side-mode frequencies, i.e., $\tilde{\Delta} = -\Omega_m = -(\Omega_c + \Omega_d)/2$. This choice of the cavity detuning allows us to elicit the signatures of both single (nonrotating BEC) as well as double-OMIT (rotating BEC) resonances from our system, as explained below. In Fig. 2(a), we plot the bistable behavior of the system for different values of control laser power [53]. We see that the system displays bistability for a few femtowatts of input power for a red-detuned control field. We further plot the dynamical stability of the system in Fig. 2(b), as indicated by the Routh-Hurwitz criterion [21]. As can be seen from the plot, for control powers $P_{lc} \ll 6$ fW, and $0 \leqslant L_p \leqslant 10$, the system is dynamically stable. Furthermore, the characteristic analytical expression for the critical control power at $\tilde{\Delta} = -\Omega_m$ is given by

$$\tilde{P}_{lc_{cr}} = \frac{\hbar\omega_{lc}\Omega_m}{54\mu\gamma_o C}\left(4\Omega_m^2 + 9\gamma_o^2\right), \tag{8}$$

where $C = G^2(\tilde{\omega}_c + \tilde{\omega}_d)/\sqrt{\mathcal{A}^2 + \Omega_c^2\Omega_d^2}$. For the remainder of our analysis, we choose parameters (for instance, $P_{lc} \ll \tilde{P}_{lc_{cr}}$ and $P_{lc} \ll 6$ fW) to keep our system away from bistability and also in the dynamically stable regime.

B. Probe transmission

To illustrate the efficacy of the system towards manipulating the coherent interference effects by atomic rotation, in what follows, we numerically simulate the probe transmission spectrum. Here we find that the atom-atom coupling strength has a negligible effect on the probe transmission and thus have set $\tilde{g} = 0$ for the rest of our analysis [21].

1. OMIT

In the absence of atomic rotation ($L_p = 0$), the two mechanical side modes are degenerate. In the presence of the control beam, the probe transmission spectrum obtained from Eq. (7) shows signatures of OMIT [24], as shown in Fig. 3(a). This is because the simultaneous presence of the control and probe fields causes the radiation pressure force to oscillate at a beat frequency $\delta = \omega_{lp} - \omega_{lc}$. If these oscillations are in resonance with Ω_m, then the mechanical side mode also starts vibrating coherently. This further gives rise to the Stokes ($\omega_{lc} - \Omega_m$) and anti-Stokes ($\omega_{lc} + \Omega_m$) scattered light from the strong control field [see Fig. 1(b)]. At $\tilde{\Delta} = -\Omega_m$, the Stokes scattering becomes highly off-resonant and gets suppressed. Thus only anti-Stokes light builds up in the cavity which is degenerate with the probe field. The destructive interference between the probe and the anti-Stokes scattering hinders the formation of the intracavity probe field and produces transparency [29,53].

The physical origin of the OMIT can also be understood from the Λ-type energy level structure for $L_p = 0$ shown in

the left half of Fig. 3(b). In this configuration, the probe field excites a direct transition $|1\rangle \leftrightarrow |3\rangle$ in which the occupation of the mechanical oscillator remains unchanged. However, the control laser is scanned close to the red sideband on an indirect transition ($|2\rangle \leftrightarrow |3\rangle$). In this transition, a mechanical excitation quantum is annihilated, and a photon is created inside the cavity. Since the control laser is much stronger than the probe, the magnitude of excitation amplitude of the indirect transition is of the same order as the direct transition. Under resonant conditions ($\delta = \Omega_m$ and $\tilde{\Delta} = -\Omega_m$), the excitation amplitude of the indirect pathway is π out of phase ($|2\rangle \rightarrow |3\rangle$ and $|3\rangle \rightarrow |2\rangle$ each contribute a $\pi/2$ phase shift) with respect to the direct excitation pathway. In other words, the two excitation pathways, $|1\rangle \rightarrow |3\rangle$ and $|1\rangle \rightarrow |3\rangle \rightarrow |2\rangle \rightarrow |3\rangle$, interfere destructively to create transparency for the probe field [54].

It is to be noted that the above interference effects are typically classical and are studied in the linearized regime where quantum nonlinear effects [55–57] are neglected. In this regime, the OMIT response is determined by a combined parameter $G|\alpha_s|$. Furthermore, such classical OMIT is typically studied in the regime $\gamma_m \ll \Gamma_{\rm opt}$ (with $\Gamma_{\rm opt} = \frac{4G^2|\alpha_s|^2}{\gamma_o}$), and $G|\alpha_s| \ll \gamma_o \ll \Omega_m$ such that the width of the OMIT window is $\Gamma_{\rm opt}$.

Since this degree of interference can be controlled by the power of the control laser, the features of the OMIT, such as the height and width of the transmission window, can also be manipulated by varying the control field power [see Fig. 3(a)]. In particular, the peak value of OMIT is saturated, and the transmission window broadens with increase in the control beam power. To quantify this, from Eq. (7), we write the following approximate expressions for the peak value and width of OMIT [25]:

$$T(\delta = \Omega_m) \approx \left(\frac{\mathcal{C}}{1+\mathcal{C}}\right)^2, \tag{9}$$

$$\Gamma_m \approx \gamma_m(1+\mathcal{C}), \tag{10}$$

where $\mathcal{C} = \frac{4G^2|\alpha_s|^2}{\gamma_o\gamma_m}$ is the system cooperativity. These analytical expressions for the peak height and width of the OMIT window both fit well with the numerical data, as shown in Fig. 4. Clearly, the peak value is saturated, and the width of the transmission window has a linear dependence on the power of the control beam.

For an initially nonrotating BEC ($L_p = 0$), the Bragg-scattered mechanical modes become degenerate and the probe transmission spectrum exhibits OMIT in the presence of a control laser. However, in the presence of a persistent flow in the ring BEC ($L_p \neq 0$), the mechanical side modes no longer remain degenerate and acquire distinguishable frequencies. This in turn modifies the output probe transmission spectrum, as shown in Fig. 5(a). Specifically, the spectrum shows double OMIT, i.e., two transparency windows emerge along with the absorption window of width $\sim|\Omega_c - \Omega_d|$ situated at $\delta = \Omega_m$ [27]. Furthermore, it can be seen that the two transmission peaks are situated at $\delta_+ = \Omega_d$ and $\delta_- = \Omega_c$, respectively. Here $\delta_+(\delta_-)$ is the position of the peak in the positive (negative) direction of Ω_m.

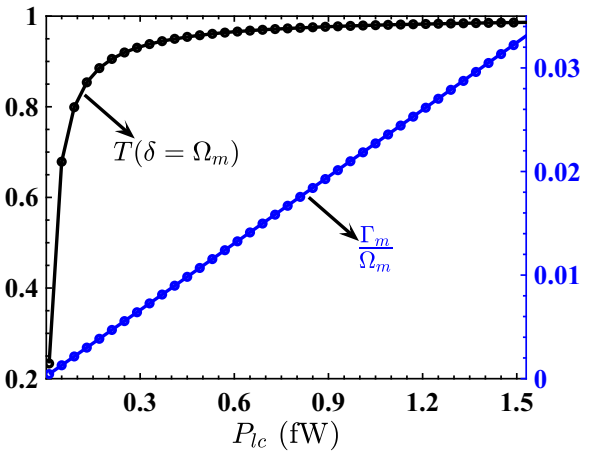

FIG. 4. Transmission T (black, left axis) of the probe field at $\delta = \Omega_m$ and width of the OMIT window Γ_m (blue, right axis) as a function of control field power. Here the solid circles represent the numerical values of the transmission and linewidth obtained from Fig. 3(a). The solid curves represent the analytical solutions from Eqs. (9) and (10). The rest of the parameters are the same as in Fig. 3.

The underlying mechanism for the above double-OMIT structure can be explained from the interference between three transition pathways formed for $L_p \neq 0$ in the double-Λ configuration as shown in the right half of Fig. 3(b). Similar to

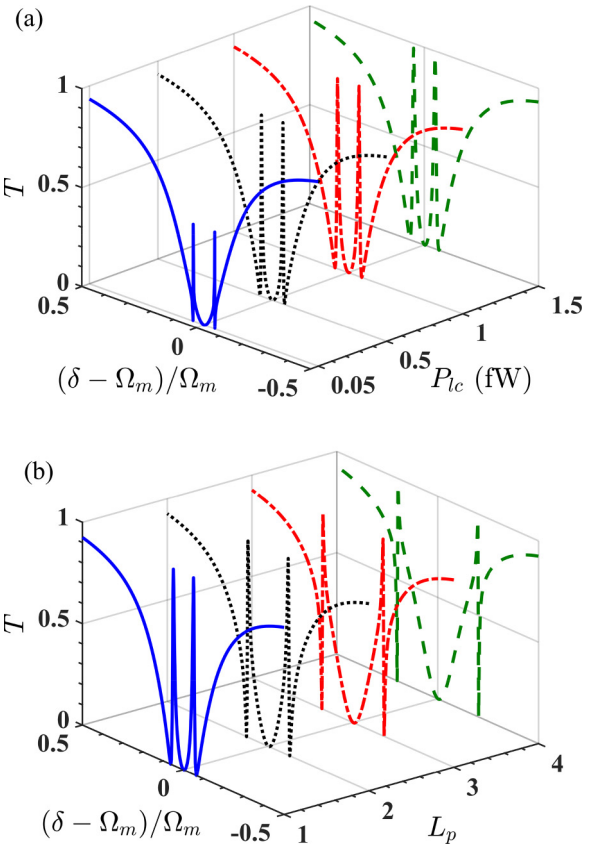

FIG. 5. (a) Probe transmission as a function of pump-probe detuning and control field power for $L_p = 1$. For this case the critical power is $\tilde{P}_{lc_{cr}} = 33$ fW. (b) Transmission of the probe field as a function of the winding number and pump-probe detuning for $P_{lc} = 1$ fW.

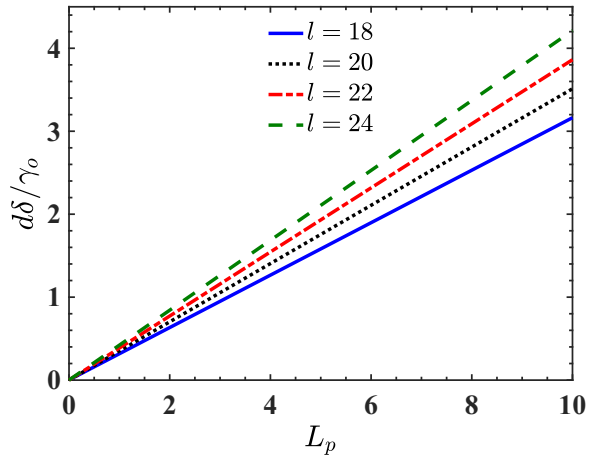

FIG. 6. Separation between the transparency peaks ($d\delta$) obtained from Fig. 5(b) as a function of the winding numbers (L_p) at control laser detuning $\tilde{\Delta} = -\Omega_m$ and for different values of OAM. The rest of the parameters are the same as in Fig. 5.

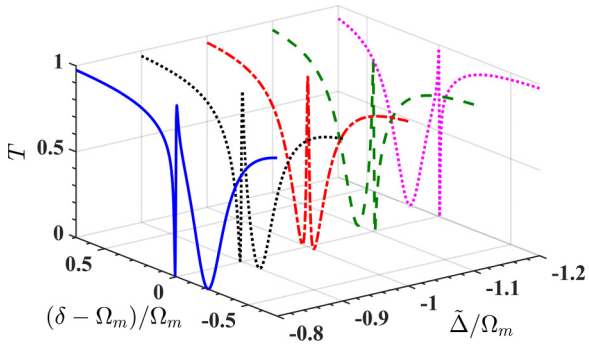

FIG. 7. Asymmetric Fano profiles obtained for $L_p = 0$ as a function of the pump-probe detuning and cavity detuning. Here, $P_{lc} = 1$ fW, and the rest of the parameters are the same as in Fig. 3.

the case of $L_p = 0$, here, the destructive interference due to π phase shift between the excitation pathways—(i) $|1\rangle \rightarrow |3\rangle$ and $|1\rangle \rightarrow |3\rangle \rightarrow |2_c\rangle \rightarrow |3\rangle$ or (ii) $|1\rangle \rightarrow |3\rangle$ and $|1\rangle \rightarrow |3\rangle \rightarrow |2_d\rangle \rightarrow |3\rangle$—suppresses the buildup of the intracavity field at the respective beat frequencies. Thus, whenever the two side-mode frequencies (at energy levels $|2_c\rangle$ and $|2_d\rangle$) are resonant with the beat frequency δ, a transparency window is observed, resulting in a double-OMIT structure [27]. However, a complete absorption at $\delta = \Omega_m$ results from the constructive interference between one direct pathway ($|1\rangle \rightarrow |3\rangle$) and two indirect excitation pathways ($|1\rangle \rightarrow |3\rangle \rightarrow |2_c\rangle \rightarrow |3\rangle$ and $|1\rangle \rightarrow |3\rangle \rightarrow |2_d\rangle \rightarrow |3\rangle$). This is because the indirect pathways give rise to a total of 2π phase shift with respect to the direct transition pathway.

The presence of persistent currents in a ring BEC modifies the probe transmission spectrum. An increase in the magnitude of the winding number of the persistent flow results in higher frequency separation between the Bragg-scattered mechanical side modes. This broadens the width of the absorption window in the double-OMIT spectrum as the winding number is increased, as shown in Fig. 5(b).

The above characteristic features of the probe transmission may serve as a tool to sense the state of rotation of the BEC. For instance, the separation of the transmission peaks from resonance increases with the BEC winding number. This dependence can be used to detect the magnitude of the winding number of the persistent flow present in the atomic superfluid. To obtain more insight, we study the separation between the transmission peaks such that $d\delta = \delta_+ - \delta_-$, as shown in Fig. 6. Salient features of this plot are as follows: (i) The peak separation varies linearly with the winding number, L_p. This is due to the fact that the transmission dips appear at frequencies $\omega_{lp} = \omega_{lc} + \Omega_c$ and $\omega_{lp} = \omega_{lc} + \Omega_d$, respectively. Thus the difference between the transmission dips varies with the beat frequency of the two mechanical side modes, which is linearly proportional to the winding number [see Fig. 5(b)]. (ii) The difference in the peak separation remains immune to the sign of the winding number (result not shown). A change in the sign of L_p is analogous to the swapping of the side-mode frequencies about their mean, resulting in equal and opposite values of frequencies, and eventually equal transmissions at resonance.

2. *Fano resonance*

Above, we have described that the coherent interference between the anti-Stokes scattering and the probe field produces salient features of OMIT. This happens when the cavity ($\tilde{\Delta}$) and pump-probe (δ) detunings become resonant with the mechanical frequency, Ω_m. Another related interference effect is the Fano profile which emerges under nonresonant anti-Stokes scattering, namely, when the cavity offset no longer remains equal to the mechanical frequency: $\tilde{\Delta} \neq -\Omega_m$.

First, we present tunable Fano resonances in the absence of quantized circulation ($L_p = 0$). Figure 7 shows the asymmetric Fano line shapes located at $\delta = \Omega_m$ and obtained by tuning the cavity detuning. Clearly, asymmetry in the transmission profile reduces as resonant detuning is approached, and eventually it disappears at $\tilde{\Delta} = -\Omega_m$, where OMIT occurs.

In the presence of quantized circulation ($L_p \neq 0$) in the ring BEC, the Bragg-scattered mechanical side modes become nondegenerate, and for $\tilde{\Delta} = -\Omega_m$ the probe transmission shows characteristic peaks at the frequencies of the mechanical oscillators, $\delta \approx \Omega_c$ and Ω_d; see Fig. 5. However, the probe transmission profile also shows interesting Fano features for off-resonant cavity detuning, i.e., $\tilde{\Delta} \neq -\Omega_m$. To illustrate this, in Fig. 8, we show the probe transmission for nonzero winding numbers and different cavity detunings. Figure 8(a) depicts the case for $L_p = 1$. When the cavity detuning is scanned on the left side ($-\tilde{\Delta} < \Omega_m$) of the resonance, then there is asymmetry in the transmission, and the resulting Fano profile is attributed to the peak present at $\delta \approx \Omega_c$, since for $-\tilde{\Delta} < \Omega_m$, the mechanical side mode of frequency Ω_d has a negligible contribution to the probe transmission. Finally, the asymmetry gradually disappears at resonance ($\tilde{\Delta} = -\Omega_m$). Furthermore, if the cavity is detuned again such that $-\tilde{\Delta} > \Omega_m$, then the Fano profiles in the probe transmission mainly occur due to the peak present at $\delta \approx \Omega_d$. In this case the contribution from Ω_c is negligible.

Fano profiles can therefore be manipulated by changing the winding number. This is shown in Fig. 8(b), where transmission is plotted at $\tilde{\Delta} = -1.2\Omega_m$ for various values of L_p.

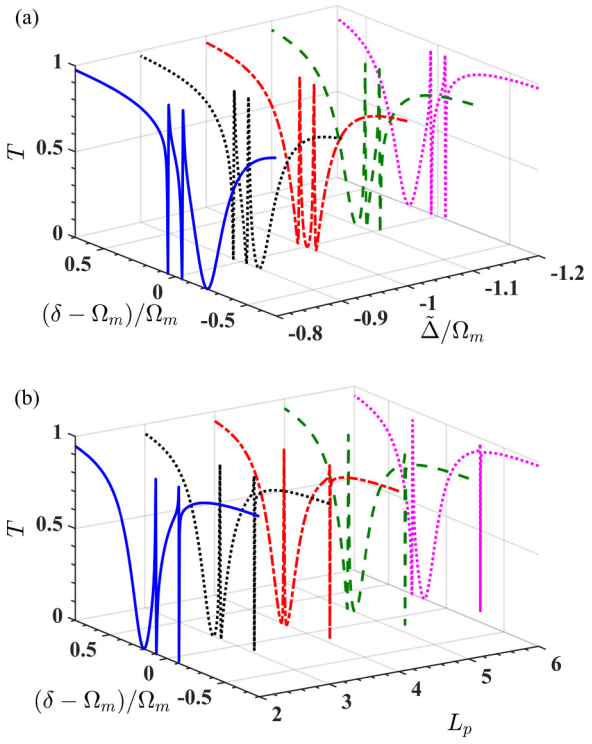

FIG. 8. (a) Probe transmission as a function of pump-probe detuning and cavity detuning for $L_p = 1$. (b) Transmission of the probe field obtained at $\tilde{\Delta} = -1.2\Omega_m$ as a function of the winding number and pump-probe detuning. Here, $P_{lc} = 1$ fW, and the other parameters are the same as in Fig. 5.

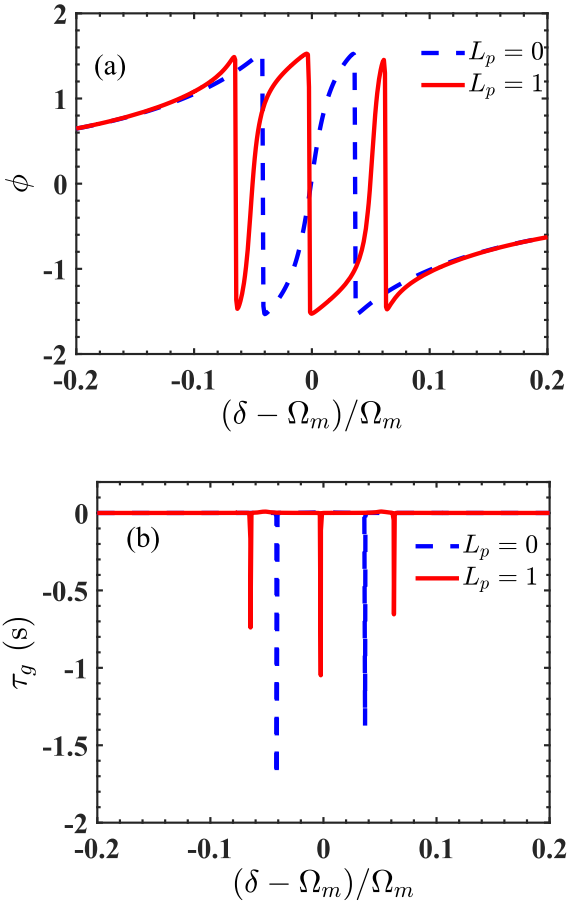

FIG. 9. (a) Transmission phase and (b) group delay as a function of pump-probe detuning. Here, $L_p = 0$ (dashed blue curve) and $L_p = 1$ (solid red curve). The parameters used are the same as in Fig. 5.

Clearly, an increase in winding number results in an increase in the frequency separation between absorption dips. This is simply due to the modification of the mechanical side-mode frequencies by the winding number of the condensate.

C. Group delay

In the preceding section, we have exploited the control-beam-generated destructive interference to obtain narrow transmission windows in the probe output spectrum. Another remarkable effect in this system is the dispersion, which allows the use of a transparency window for the exploration of slow or fast light. Specifically, it is the rapid variation of the transmission phase of the probe field within the transparency window which governs the dispersion. From Eq. (6), such a transmission phase dispersion profile is obtained as $\phi(\omega_{lp}) = \arg[t_S(\omega_{lp})]$, and its slope is related to the corresponding transmission group delay by [58]

$$\tau_g = \frac{d\phi(\omega_{lp})}{d\omega_{lp}}. \tag{11}$$

Figure 9 displays the transmission phase and group delay as a function of pump-probe detuning in the absence and presence of quantized circulation. Around resonance, $\delta = \Omega_m$, the transmission phase of the probe field shows a rapid positive (negative) variation for $L_p = 0$ ($L_p = 1$), as shown in Fig. 9(a). This suggests that within the transparency window, switching from positive group delay (slow light) to negative group delay (fast light) takes place once the BEC starts rotating, as exhibited in Fig. 9(b). For instance, at $\delta = \Omega_m$, the group delay for $L_p = 0$ is 4.2 ms, whereas for $L_p = 1$ its value is -1.05 s.

As per Eq. (11), the variation of the transmission phase at resonance plays an important role in determining the group delay. In Fig. 10(a), we exhibit the group delay at $\delta = \Omega_m$, as a function of the power of the control beam for different winding numbers. For $L_p = 0$, group delay decreases with control power, as shown in the inset of Fig. 10(a). This is because for lower power the transmission window is very narrow [see Fig. 3(a)] and therefore the corresponding dispersion profile has a very sharp slope around resonance which corresponds to high group index and slow light. However, with an increase in power, the transmission window broadens, and eventually the slope of the dispersion decreases. This results in a decrease in the group delay and an increase in the speed of light. An approximate analytic expression of the group delay at resonance can be obtained as [53]

$$\tau_g\Big|_{\delta=\Omega_m}^{L_p=0} = \frac{2}{\gamma_m(1+\mathcal{C})}. \tag{12}$$

This equation describes well the group index for $L_p = 0$ shown in the inset of Fig. 10(a). Now, in the presence of atomic circulation, the group delay becomes negative corre-

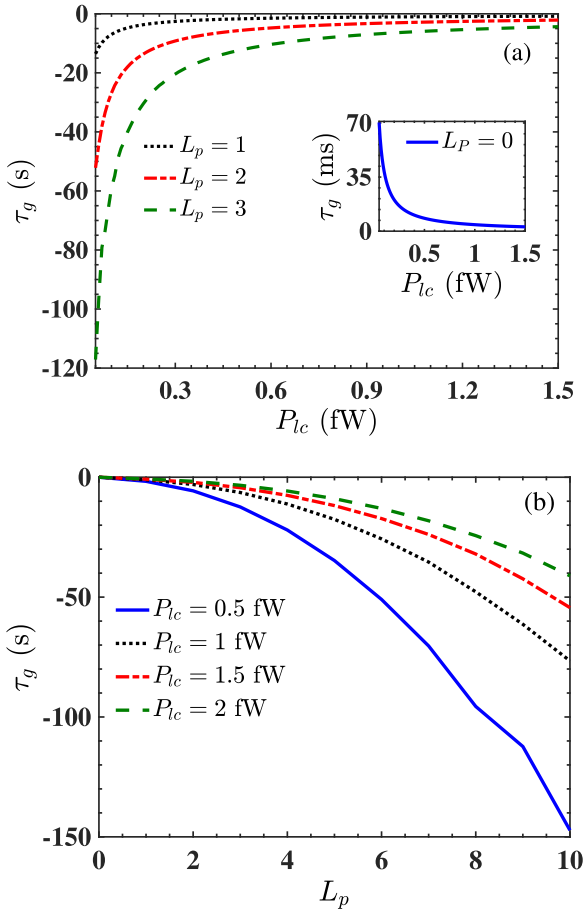

FIG. 10. Group delay as a function of (a) control power for different L_p and (b) winding number for different power values of the control beam. Here, group delay is obtained at $\delta = \Omega_m$, and the rest of the parameters are the same as in Fig. 9.

sponding to fast light. Furthermore, with increase in power the negativeness of the group delay diminishes for the same reason as explained above.

Since, with increase in the winding number, the absorption window around resonance broadens and the negativity of the slope of the dispersion profile decreases, this causes the group delay to become more negative as shown in Fig. 10(b).

IV. CONCLUSION

In conclusion, we have investigated how coherent interference effects can be manipulated by atomic persistent currents interacting with control and probe fields inside an optical resonator. First, we analyzed the transmission spectrum of the probe field in the presence of a control beam. The system shows narrow transmission profiles due to interference between the probe and control beams, mediated by the condensate. Specifically, we have described OMIT and double-OMIT resonance transmission profiles in the absence and presence of quantized circulation, respectively. Interestingly, the separation between the absorption dips in the double-OMIT structure provides information about the magnitude of the winding number. Furthermore, for nonresonant conditions, the probe transmission spectrum becomes asymmetric due to Fano resonances which are also influenced by the atomic circulation of the annularly trapped BEC. Apart from the probe transmission, we have also presented the manipulation of the group delay of the probe field. Remarkably, the system has shown switching from slow to fast light as atomic circulation is turned on. The observed phenomena can be employed to utilize coherent matter waves for the realization of optical switches [59], sensing [60], and processing, storage, and retrieval of information [61].

ACKNOWLEDGMENTS

S.K. gratefully acknowledges the support of MHRD, Government of India, for funding his research through the PMRF scheme. P.K. acknowledges the Max Planck Society for financial support. M.B. acknowledges an NSF Career award (Directorate for Mathematical and Physical Sciences, Award No. 1454931). R.K. acknowledges support from JSPS KAKENHI Grant No. JP21K03421 and JST CREST Grant No. JPMJCR1771.

[1] S. Beattie, S. Moulder, R. J. Fletcher, and Z. Hadzibabic, Persistent Currents in Spinor Condensates, Phys. Rev. Lett. **110**, 025301 (2013).

[2] K. C. Wright, R. B. Blakestad, C. J. Lobb, W. D. Phillips, and G. K. Campbell, Driving Phase Slips in a Superfluid Atom Circuit with a Rotating Weak Link, Phys. Rev. Lett. **110**, 025302 (2013).

[3] C. Ryu, P. W. Blackburn, A. A. Blinova, and M. G. Boshier, Experimental Realization of Josephson Junctions for an Atom SQUID, Phys. Rev. Lett. **111**, 205301 (2013).

[4] S. Eckel, J. G. Lee, F. Jendrzejewski, N. Murray, C. W. Clark, C. J. Lobb, W. D. Phillips, M. Edwards, and G. K. Campbell, Hysteresis in a quantized superfluid 'Atomtronic' circuit, Nature (London) **506**, 200 (2014).

[5] G. E. Marti, R. Olf, and D. M. Stamper-Kurn, Collective excitation interferometry with a toroidal Bose-Einstein condensate, Phys. Rev. A **91**, 013602 (2015).

[6] S. Eckel, A. Kumar, T. Jacobson, I. B. Spielman, and G. K. Campbell, A Rapidly Expanding Bose-Einstein Condensate: An Expanding Universe in the Lab, Phys. Rev. X **8**, 021021 (2018).

[7] P. Öhberg and E. M. Wright, Quantum Time Crystals and Interacting Gauge Theories in Atomic Bose-Einstein Condensates, Phys. Rev. Lett. **123**, 250402 (2019).

[8] A. L. Fetter, Rotating trapped Bose-Einstein condensates, Rev. Mod. Phys. **81**, 647 (2009).

[9] D. V. Freilich, D. M. Bianchi, A. M. Kaufman, T. K. Langin, and D. S. Hall, Real-time dynamics of single vortex lines and vortex dipoles in a Bose-Einstein condensate, Science **329**, 1182 (2010).

[10] C. Ryu, M. F. Andersen, P. Cladé, V. Natarajan, K. Helmerson, and W. D. Phillips, Observation of Persistent Flow of a Bose-Einstein Condensate in a Toroidal Trap, Phys. Rev. Lett. **99**, 260401 (2007).

[11] N. R. Cooper, Rapidly rotating atomic gases, Adv. Phys. **57**, 539 (2008).

[12] Y. Shin, M. Saba, M. Vengalattore, T. A. Pasquini, C. Sanner, A. E. Leanhardt, M. Prentiss, D. E. Pritchard, and W. Ketterle, Dynamical Instability of a Doubly Quantized Vortex in a Bose-Einstein Condensate, Phys. Rev. Lett. **93**, 160406 (2004).

[13] D. R. Tilley and J. Tilley, *Superfluidity and Superconductivity* (Routledge, Milton Park, UK, 2019).

[14] Z. Mehdi, A. S. Bradley, J. J. Hope, and S. S. Szigeti, Superflow decay in a toroidal Bose gas: The effect of quantum and thermal fluctuations, SciPost Phys. **11**, 080 (2021).

[15] S. Pandey, H. Mas, G. Vasilakis, and W. von Klitzing, Atomtronic Matter-Wave Lensing, Phys. Rev. Lett. **126**, 170402 (2021).

[16] L. Amico, M. Boshier, G. Birkl, A. Minguzzi, C. Miniatura, L.-C. Kwek, D. Aghamalyan, V. Ahufinger, D. Anderson, N. Andrei, A. S. Arnold, M. Baker, T. A. Bell, T. Bland, J. P. Brantut, D. Cassettari, W. J. Chetcuti, F. Chevy, R. Citro, S. De Palo *et al.*, Roadmap on atomtronics: State of the art and perspective, AVS Quantum Sci. **3**, 039201 (2021).

[17] J. Polo, V. Ahufinger, F. W. J. Hekking, and A. Minguzzi, Damping of Josephson Oscillations in Strongly Correlated One-Dimensional Atomic Gases, Phys. Rev. Lett. **121**, 090404 (2018).

[18] J. W. Park, B. Ko, and Y. Shin, Critical Vortex Shedding in a Strongly Interacting Fermionic Superfluid, Phys. Rev. Lett. **121**, 225301 (2018).

[19] Y. Cai, D. G. Allman, P. Sabharwal, and K. C. Wright, Persistent Currents in Rings of Ultracold Fermionic Atoms, Phys. Rev. Lett. **128**, 150401 (2022).

[20] G. Del Pace, K. Xhani, A. M. Falconi, M. Fedrizzi, N. Grani, D. H. Rajkov, M. Inguscio, F. Scazza, W. J. Kwon, and G. Roati, Imprinting Persistent Currents in Tunable Fermionic Rings, Phys. Rev. X **12**, 041037 (2022).

[21] P. Kumar, T. Biswas, K. Feliz, R. Kanamoto, M.-S. Chang, A. K. Jha, and M. Bhattacharya, Cavity Optomechanical Sensing and Manipulation of an Atomic Persistent Current, Phys. Rev. Lett. **127**, 113601 (2021).

[22] M. Aspelmeyer, T. J. Kippenberg, and F. Marquardt, Cavity optomechanics, Rev. Mod. Phys. **86**, 1391 (2014).

[23] H. Shi and M. Bhattacharya, Optomechanics based on angular momentum exchange between light and matter, J. Phys. B: At. Mol. Opt. Phys. **49**, 153001 (2016).

[24] G. S. Agarwal and S. Huang, Electromagnetically induced transparency in mechanical effects of light, Phys. Rev. A **81**, 041803(R) (2010).

[25] S. Weis, R. Rivière, S. Deléglise, E. Gavartin, O. Arcizet, A. Schliesser, and T. J. Kippenberg, Optomechanically induced transparency, Science **330**, 1520 (2010).

[26] A. H. Safavi-Naeini, T. P. M. Alegre, M. Eichenfield, M. Wigner, Q. Lin, J. T. Hill, D. E. Chang, and O. Painter, Electromagnetically induced transparency and slow light with optomechanics, Nature (London) **472**, 69 (2011).

[27] P.-C. Ma, J.-Q. Zhang, Y. Xiao, M. Feng, and Z.-M. Zhang, Tunable double optomechanically induced transparency in an optomechanical system, Phys. Rev. A **90**, 043825 (2014).

[28] S. Huang, Double electromagnetically induced transparency and narrowing of probe absorption in a ring cavity with nanomechanical mirrors, J. Phys. B: At. Mol. Opt. Phys. **47**, 055504 (2014).

[29] J.-X. Peng, Z. Chen, Q.-Z. Yuan, and X.-L. Feng, Double optomechanically induced transparency in a Laguerre-Gaussian rovibrational cavity, Phys. Lett. A **384**, 126153 (2020).

[30] S. E. Harris, Lasers Without Inversion: Interference of Lifetime-Broadened Resonances, Phys. Rev. Lett. **62**, 1033 (1989).

[31] S. E. Harris, J. E. Field, and A. Imamoğlu, Nonlinear Optical Processes Using Electromagnetically Induced Transparency, Phys. Rev. Lett. **64**, 1107 (1990).

[32] K.-J. Boller, A. Imamoğlu, and S. E. Harris, Observation of Electromagnetically Induced Transparency, Phys. Rev. Lett. **66**, 2593 (1991).

[33] J. P. Marangos, Electromagnetically induced transparency, J. Mod. Opt. **45**, 471 (1998).

[34] K. Qu and G. S. Agarwal, Fano resonances and their control in optomechanics, Phys. Rev. A **87**, 063813 (2013).

[35] H.-J. Chen, Multiple-Fano-resonance-induced fast and slow light in the hybrid nanomechanical-resonator system, Phys. Rev. A **104**, 013708 (2021).

[36] L. Tian, Adiabatic State Conversion and Pulse Transmission in Optomechanical Systems, Phys. Rev. Lett. **108**, 153604 (2012).

[37] Y.-D. Wang and A. A. Clerk, Using Interference for High Fidelity Quantum State Transfer in Optomechanics, Phys. Rev. Lett. **108**, 153603 (2012).

[38] Z. Zhang, J. Pei, Y.-P. Wang, and X. Wang, Measuring orbital angular momentum of vortex beams in optomechanics, Front. Phys. **16**, 32503 (2021).

[39] L. Stern, M. Grajower, and U. Levy, Fano resonances and all-optical switching in a resonantly coupled plasmonic-atomic system, Nat. Commun. **5**, 4865 (2014).

[40] H. Lü, Y. Jiang, Y.-Z. Wang, and H. Jing, Optomechanically induced transparency in a spinning resonator, Photonics Res. **5**, 367 (2017).

[41] J. T. Hill, A. H. Safavi-Naeini, J. Chan, and O. Painter, Coherent optical wavelength conversion via cavity optomechanics, Nat. Commun. **3**, 1196 (2012).

[42] O. Morizot, Y. Colombe, V. Lorent, H. Perrin, and B. M. Garraway, Ring trap for ultracold atoms, Phys. Rev. A **74**, 023617 (2006).

[43] D. Naidoo, K. Aït-Ameur, M. Brunel, and A. Forbes, Intracavity generation of the superpositions of Laguerre-Gaussian beams, Appl. Phys. B **106**, 683 (2012).

[44] Z. D. Cheng, Z. D. Liu, X. W. Luo, Z. W. Zhou, J. Wang, Q. Li, Y. T. Wang, J. S. Tang, J. S. Xu, C. F. Li, and G. C. Guo, Degenerate cavity supporting more than 31 Laguerre-Gaussian modes, Opt. Lett. **42**, 2042 (2017).

[45] S. Huang, Z. Miao, C. He, F. Pang, Y. Li, and T. Wang, Composite vortex beams by coaxial superposition of Laguerre–Gaussian beams, Opt. Lasers Eng. **78**, 132 (2016).

[46] S. Moulder, S. Beattie, R. P. Smith, N. Tammuz, and Z. Hadzibabic, Quantized supercurrent decay in an annular Bose-Einstein condensate, Phys. Rev. A **86**, 013629 (2012).

[47] W. P. Bowen and G. J. Milburn, *Quantum Optomechanics* (Taylor & Francis, London, 2015).

[48] F. Brennecke, S. Ritter, T. Donner, and T. Esslinger, Cavity optomechanics with a Bose-Einstein condensate, Science **322**, 235 (2008).

[49] M. de G. de Herve, Y. Guo, C. De Rossi, A. Kumar, T. Badr, R. Dubessy, L. Longchambon, and H. Perrin, A versatile ring trap for quantum gases, J. Phys. B: At. Mol. Opt. Phys. **54**, 125302 (2021).

[50] E. Tiesinga, C. J. Williams, P. S. Julienne, K. M. Jones, P. D. Lett, and W. D. Phillips, A spectroscopic determination of scattering lengths for sodium atomic collisions, J. Res. Natl. Inst. Stand. Technol. **101**, 505 (1996).

[51] A. D. Ludlow, X. Huang, M. Notcutt, T. Zanon-Willette, S. M. Foreman, M. M. Boyd, S. Blatt, and J. Ye, Compact, thermal-noise-limited optical cavity for diode laser stabilization at 1×10^{-15}, Opt. Lett. **32**, 641 (2007).

[52] E. X. DeJesus and C. Kaufman, Routh-Hurwitz criterion in the examination of eigenvalues of a system of nonlinear ordinary differential equations, Phys. Rev. A **35**, 5288 (1987).

[53] H. Xiong and Y. Wu, Fundamentals and applications of optomechanically induced transparency, Appl. Phys. Rev. **5**, 031305 (2018).

[54] C. L. Garrido Alzar, M. A. G. Martinez, and P. Nussenzveig, Classical analog of electromagnetically induced transparency, Am. J. Phys. **70**, 37 (2002).

[55] A. Kronwald and F. Marquardt, Optomechanically Induced Transparency in the Nonlinear Quantum Regime, Phys. Rev. Lett. **111**, 133601 (2013).

[56] K. Børkje, A. Nunnenkamp, J. D. Teufel, and S. M. Girvin, Signatures of Nonlinear Cavity Optomechanics in the Weak Coupling Regime, Phys. Rev. Lett. **111**, 053603 (2013).

[57] M. A. Lemonde, N. Didier, and A. A. Clerk, Nonlinear Interaction Effects in a Strongly Driven Optomechanical Cavity, Phys. Rev. Lett. **111**, 053602 (2013).

[58] H. Mikaeili, A. Dalafi, M. Ghanaatshoar, and B. Askari, Ultraslow light realization using an interacting Bose-Einstein condensate trapped in a shallow optical lattice, Sci. Rep. **12**, 4428 (2022).

[59] A. Dreismann, H. Ohadi, Y. del Valle-Inclan Redondo, R. Balili, Y. G. Rubo, S. I. Tsintzos, G. Deligeorgis, Z. Hatzopoulos, P. G. Savvidis, and J. J. Baumberg, A sub-femtojoule electrical spin-switch based on optically trapped polariton condensates, Nat. Mater. **15**, 1074 (2016).

[60] G. Pelegrí, J. Mompart, and V. Ahufinger, Quantum sensing using imbalanced counter-rotating Bose–Einstein condensate modes, New J. Phys. **20**, 103001 (2018).

[61] T. Chanelière, D. N. Matsukevich, S. D. Jenkins, S.-Y. Lan, T. A. B. Kennedy, and A. Kuzmich, Storage and retrieval of single photons transmitted between remote quantum memories, Nature (London) **438**, 833 (2005).